Editors' Suggestion | Featured in Physics

Interference-Induced Entanglement Engineering on a Metasurface

Yajun Gao,[1,*] Rui Zhong,[1,*] Xianglin Mao,[1,*] Hulin Zhang,[1] Yue Jiang,[1] Chenyu Bao,[1] Chuanfeng Li,[2] Ruwen Peng,[1,†] and Mu Wang[1,‡]

[1]*National Laboratory of Solid State Microstructures, School of Physics, and Collaborative Innovation Center of Advanced Microstructures, Nanjing University, Nanjing 210093, China*

[2]*CAS Key Laboratory of Quantum Information, University of Science and Technology of China, Hefei 230026, China*

(Received 12 October 2024; revised 30 August 2025; accepted 14 November 2025; published 13 January 2026)

Conventional approaches to generating and distributing entangled quantum states usually rely on bulky traditional optical devices, posing significant challenges to system miniaturization and integration. Here we report an entanglement engineering scheme that utilizes quantum interference on a metasurface, combined with postselection, to generate and distribute multiple polarization-entangled photon pairs. Two unentangled identical photons, differing only in polarization, are incident on a multichannel metasurface where each channel supports a specific polarization transformation. The metasurface facilitates two-photon interference, generating postselected polarization-entangled states and forming a fully connected entanglement distribution among every two output channels. Experiments demonstrate the generation and distribution of four Bell states across 21 channel pairs, underscoring the potential of metasurfaces as compact, scalable entanglement sources for quantum networking.

DOI: 10.1103/mzmv-7x98

Quantum entanglement is the basis of information processing in quantum operations [1–5]. Generation and modulation of Bell states [6] in two-dimensional Hilbert space have drawn much attention due to their wide applications in quantum key distribution [3,7], teleportation [1,8], dense coding [9,10], and secret sharing [11,12]. On the other hand, quantum networking demands remote distribution of entanglement among different users [13–16]. A typical scheme for generating and distributing multiple polarization-entangled photon states consists of three main components: a polarization-entangled photon source [17–21], state transformation optics [22,23], and entanglement distribution modules [24,25]. However, such systems currently rely on numerous bulky and discrete optical components, presenting significant challenges for scalability and integration. The photon source is commonly based on spontaneous parametric down-conversion (SPDC) in a nonlinear crystal operating under quasi-phase-matching conditions, which enables the generation of photon pairs with high brightness [21,26]. Achieving polarization entanglement typically requires either combining two orthogonally oriented nonlinear crystals [27,28], embedding the crystals in a Sagnac interferometer composed of polarization beam splitters (PBS) and a half-wave plate (HWP) [29,30], or employing postselection via coincidence detection after interfering photon pairs on beam splitters [31–33]. State transformation is then carried out using combinations of quarter-wave plates (QWPs) and HWPs to tailor the entangled states as needed. Finally, entanglement distribution is achieved using components such as beam splitters [34,35], optical switches [36,37], and wavelength-division multiplexing systems [38]. Despite their essential roles, these discrete optical elements are fundamentally incompatible with the integration and miniaturization demands for future quantum networks.

So far, as a promising candidate for integrating and miniaturizing conventional optical systems, a specially designed metasurface enables the generation and detection of multiphoton states in a compact space [39–47]. For example, nonlinear metasurfaces supporting nonlocal resonances generate photon pairs via SPDC [44,45]. The metalens array enables a high-dimensional entangled photon source [42]. Metasurfaces also realize multiphoton interferences [41,43] and quantum state measurements [40,47]. To distribute entangled photon pairs, we once introduced two metasurfaces based on the geometrical-scaling-induced (GSI) phase modulation [46]. Each photon of the entangled pair interacts with one metasurface possessing multiple output channels, where unitary transformations result in various photon states. However, in [46] the incidence comes from an entangled light source, and on the output side, the entanglement exists only between the output channels from different metasurfaces. In contrast, the photons emitted from the output channels of the same metasurface are not entangled, raising significant challenges to optimizing efficiency, scalability, and resource utilization in a network. A single metasurface that enables

*These authors contributed equally to this work.
†Contact author: rwpeng@nju.edu.cn
‡Contact author: muwang@nju.edu.cn

entanglement generation, transformation, and fully connected distribution is highly desirable for constructing an integrated quantum network; yet, its realization remains challenging.

In this Letter, we experimentally demonstrate the generation, transformation, and distribution of polarization entanglement using a single metasurface. We exploit quantum interference on a specially designed N-channel metasurface with a GSI phase gradient to generate and distribute polarization-entangled two-photon states among $N(N-1)/2$ pairs of output channels. Experimentally, two photons with orthogonal linear polarization align on a seven-channel ($N=7$) metasurface and convert into four Bell states $[(|HV\rangle \pm |VH\rangle)/\sqrt{2}$ $(\Psi^{\pm})$ and $(|HH\rangle \pm |VV\rangle)/\sqrt{2}$ $(\phi^{\pm})]$ via postselection and distribute them across 21 pairs of output channels. It confirms that a single metasurface can generate multiple spatially distributed entangled photon states, which is enlightening for the development of integrated quantum networks.

Figure 1 designates how a metasurface modulates photon entanglement. The unit cell of the metasurface is composed of eight silicon nanocuboids with different sizes, aspect ratios, and orientations, which are grouped into two subsets $\{P_{(2j-1)}\}$ and $\{P_{2j}\}$ ($j=1, 2, 3, 4$) illustrated as orange and purple blocks, respectively. The orientations of structures in the subset $\{P_{(2j-1)}\}$ are either 0 or $\pi/2$, and those in $\{P_{2j}\}$ are $\pi/4$ or $3\pi/4$. A nanocuboid adds additional phase ϕ and $\phi+\Delta\phi$ to the scattered field when the polarization of the incident light is parallel and orthogonal to the symmetrical axis of the nanocuboid, respectively. The additional phases are determined by the geometry of nanocuboids [48,49]. The nanocuboids in the unit cell are so designed that 7 ($N=7$) output channels (CH_1, $CH_2, \ldots, CH_7$ corresponding to -3rd, -2nd, …, 2nd, 3rd diffraction orders) are generated, and each channel is represented by a Jones matrix $\hat{J}_m$ with $m=1,2,\ldots,7$. Furthermore, the nanocuboids in $\{P_{(2j-1)}\}$ possess a phase difference π when they are $D_x/2$ apart in the unit cell (D_x is the periodicity of the unit cell in the x direction). This phase distribution makes the subset $\{P_{(2j-1)}\}$ contribute only to the odd orders in the scattered field. Similarly, we regulate the nanocuboids $D_x/2$ apart in $\{P_{2j}\}$ with the same phase arrangement, so their diffracted field contributes only to the even orders. The Jones matrix $\hat{J}_m$ of each channel follows

$$\hat{J}_m = C_m \sum_{j=1}^{8} e^{-i(2\pi j\sigma_m/8)} \left\{ R(-\theta_j) \begin{bmatrix} e^{i\phi_j} & 0 \\ 0 & e^{i(\phi_j+\Delta\phi_j)} \end{bmatrix} R(\theta_j) \right\}, \tag{1}$$

where σ_m ($\sigma_m = 0, \pm1, \pm2, \pm3$) is the diffraction order corresponding to channel CH_m, C_m is a normalized parameter related to the transmittance of the nanocuboids, wavelength, and periodicity in the x direction, and j ($j=1,2,\ldots,8$) is the index of the nanocuboid in the unit cell. Each nanocuboid satisfies $\Delta\phi_j$ equaling $\pi/2$ or $-\pi/2$. We define the rotation matrix as $R(\theta_j) = \left[\begin{smallmatrix} \cos\theta_j & \sin\theta_j \\ -\sin\theta_j & \cos\theta_j \end{smallmatrix}\right]$, where θ_j is selected as 0, $\pi/2$, $\pi/4$, or $3\pi/4$, respectively. We scan all possible combinations of the nanocuboids from the library (Fig. S2 in Supplemental Material [50]) and find that once the unit cell in Fig. 1 satisfies $\phi_1 = 5\pi/4$, $\phi_2 = 5\pi/4$, $\phi_3 = \pi/4$, $\phi_4 = 5\pi/4$, $\phi_5 = \pi/4$, $\phi_6 = 5\pi/4$, $\phi_7 = 3\pi/4$, $\phi_8 = 5\pi/4$, $\Delta\phi_1 = \Delta\phi_2 = \Delta\phi_4 = \Delta\phi_5 = \Delta\phi_6 = \Delta\phi_7 = \Delta\phi_8 = \pi/2$, $\Delta\phi_3 = -\pi/2$, $\theta_1 = \theta_3 = \theta_5 = 0$, $\theta_2 = \theta_6 = \pi/4$, $\theta_7 = \pi/2$, $\theta_4 = \theta_8 = 3\pi/4$, each channel serves as either a full wave plate (with no polarization conversion) or an HWP. Taking the concrete values of additional phases and orientations to Eq. (1), we obtain $\hat{J}_1 = \hat{J}_4 = \hat{J}_5 = \left(\begin{smallmatrix} 1 & 0 \\ 0 & 1 \end{smallmatrix}\right)$, $\hat{J}_2 = \hat{J}_6 = \left(\begin{smallmatrix} 0 & 1 \\ 1 & 0 \end{smallmatrix}\right)$, $\hat{J}_3 = \hat{J}_7 = \left(\begin{smallmatrix} 1 & 0 \\ 0 & -1 \end{smallmatrix}\right)$ [50].

The interaction of photons and the metasurface can be understood as follows. The two photons are indistinguishable in their temporal, spectral, and spatial characteristics. They are orthogonal in polarization, with one horizontally polarized $[|H\rangle = \left(\begin{smallmatrix} 1 \\ 0 \end{smallmatrix}\right)]$ and the other vertically polarized $[|V\rangle = \left(\begin{smallmatrix} 0 \\ 1 \end{smallmatrix}\right)]$. Each photon of the orthogonally polarized photon pair has 7 possible outputs. By combining every two output channels, one may compose channel pairs $PA_{m,n}$ ($m=1,2,\ldots,7$, $n=1,2,\ldots,7$). Considering the detailed form of $\hat{J}_m$, the interaction between $|H\rangle$ ($|V\rangle$) and metasurface can be represented as $|H\rangle \rightarrow (\alpha_1\hat{J}_1 + \alpha_2\hat{J}_2 + \cdots \alpha_7\hat{J}_7)|H\rangle = \alpha_1|H\rangle_1 + \alpha_2|V\rangle_2 + \alpha_3|H\rangle_3 + \alpha_4|H\rangle_4 +$

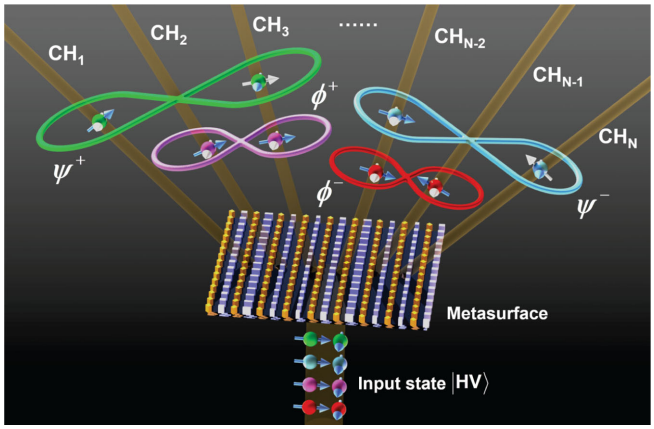

FIG. 1. Schematic of polarization entanglement transformation and distribution with a single metasurface. Two photons with orthogonal linear polarization states $|HV\rangle$ illuminate on the N-channel metasurface. The output state at each channel pair with postselection is in the Bell state $\Psi^{\pm}$ or $\phi^{\pm}$. Small spheres with the same color represent a photon pair, and the arrows across the sphere represent the linear polarization states. The white (blue) arrows on the output side represent the correlated polarization of the entangled photons. For each channel pair, once a photon is projected onto the "blue" ("white") state, the other photon will be in the "blue" ("white") state.

$\alpha_5|H\rangle_5 + \alpha_6|V\rangle_6 + \alpha_7|H\rangle_7$, $|V\rangle \rightarrow (\alpha_1\hat{J}_1 + \alpha_2\hat{J}_2 + \cdots \alpha_7\hat{J}_7)|V\rangle = \alpha_1|V\rangle_1 + \alpha_2|H\rangle_2 - \alpha_3|V\rangle_3 + \alpha_4|V\rangle_4 + \alpha_5|V\rangle_5 + \alpha_6|H\rangle_6 - \alpha_7|V\rangle_7$, where α_m is the transmission coefficient at CH_m ($m = 1, 2, \ldots, 7$), and each ket represents a specific single-photon state with subscript m denoting the output channel CH_m. The output two-photon state from the metasurface can be expressed as $(\alpha_1\hat{J}_1 + \alpha_2\hat{J}_2 + \cdots + \alpha_7\hat{J}_7)|H\rangle \otimes (\alpha_1\hat{J}_1 + \alpha_2\hat{J}_2 + \cdots + \alpha_7\hat{J}_7)|V\rangle$. When we consider a specific channel pair $PA_{m,n}$, the state is simplified as $(\alpha_m\hat{J}_m + \alpha_n\hat{J}_n)|H\rangle \otimes (\alpha_m\hat{J}_m + \alpha_n\hat{J}_n)|V\rangle$. Meanwhile, $\alpha_m\alpha_n\hat{J}_m|H\rangle \otimes \hat{J}_n|V\rangle$ and $\alpha_m\alpha_n\hat{J}_m|V\rangle \otimes \hat{J}_n|H\rangle$ correspond to two scenarios that can be experimentally postselected via the coincidence detection between two distinct channels (CH_m and CH_n), i.e., $|H\rangle$ input photon goes to CH_m, $|V\rangle$ input photon goes to CH_n, or the other way round. The indistinguishability of these two scenarios leads to interference, resulting in a Shih-Alley type polarization-entangled state [34,61] across CH_m and CH_n (Fig. 1),

$$|\Psi_{m,n}\rangle = \frac{1}{\sqrt{2}}(\hat{J}_m|H\rangle \otimes \hat{J}_n|V\rangle + \hat{J}_m|V\rangle \otimes \hat{J}_n|H\rangle), \quad (2)$$

where the coefficients have been normalized. Taking the concrete forms of $\hat{J}_m$ and $\hat{J}_n$ to Eq. (2), we can find that $|\Psi_{m,n}\rangle$ covers four Bell states ($\Psi^{\pm}$ and $\phi^{\pm}$). For example, $|\Psi_{1,5}\rangle = (|HV\rangle + |VH\rangle)/\sqrt{2}$, $|\Psi_{1,2}\rangle = (|HH\rangle + |VV\rangle)/\sqrt{2}$, $|\Psi_{1,3}\rangle = (|HV\rangle - |VH\rangle)/\sqrt{2}$, $|\Psi_{2,3}\rangle = (|HH\rangle - |VV\rangle)/\sqrt{2}$. It is noteworthy that the metasurface with 7 output channels has a total of 21 (C_7^2) channel pairs. Among them, 5 channel pairs ($PA_{1,4}$, $PA_{1,5}$, $PA_{2,6}$, $PA_{3,7}$, $PA_{4,5}$) are in $(|HV\rangle + |VH\rangle)/\sqrt{2}$, 6 pairs ($PA_{1,3}$, $PA_{1,7}$, $PA_{3,4}$, $PA_{3,5}$, $PA_{4,7}$, $PA_{5,7}$) are in $(|HV\rangle - |VH\rangle)/\sqrt{2}$, 6 pairs ($PA_{1,2}$, $PA_{1,6}$, $PA_{2,4}$, $PA_{2,5}$, $PA_{4,6}$, $PA_{5,6}$) are in $(|HH\rangle + |VV\rangle)/\sqrt{2}$, and the remaining 4 pairs ($PA_{2,3}$, $PA_{2,7}$, $PA_{3,6}$, $PA_{6,7}$) are in $(|HH\rangle - |VV\rangle)/\sqrt{2}$.

To experimentally verify the multichannel capability of the metasurface, we perform the angle-resolved coincidence measurement with a heralded single-photon source as the input [Fig. S8(a) in Supplemental Material [50]]. The photon source comprises a periodically poled $KTiOPO_4$ (PPKTP) crystal creating photon pairs with orthogonal linearly polarized states $|HV\rangle$ via SPDC. The PPKTP crystal is temperature stabilized at 40.5 °C, optimized for maximum quantum efficiency in photon-pair generation [50]. For the incident photon pair, one photon acts as the trigger for detecting the signal photon, while the other photon (the signal) passes through the metasurface with the unit cell consisting of 8 nanocuboids [Fig. 2(a)]. The input photon state can be tuned by rotating the HWP before the metasurface. To characterize the output photon state, the QWP and PBS are placed in front of the fiber coupler to project the output state. The output photon is collected directly by the single-photon counting modules

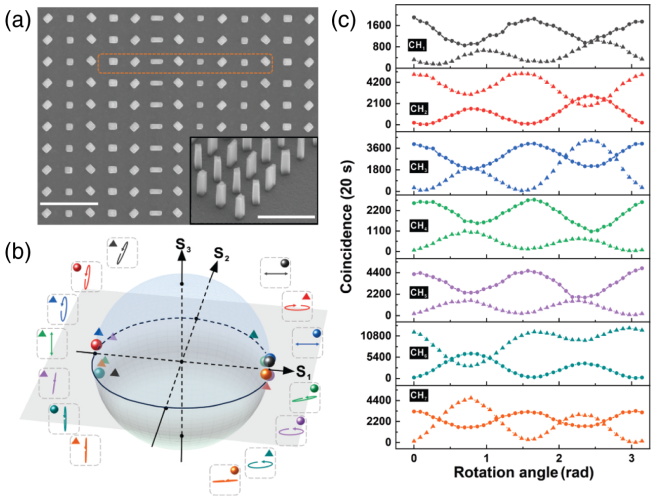

FIG. 2. (a) SEM micrographs of the fabricated metasurfaces. The dashed red box marks the unit cell. The inset is the oblique, enlarged view of the sample. The bars represent 1 μm. (b) The retrieved Stokes parameters of 7 output channels marked on the surface of the Poincaré sphere when the input single-photon states are $|H\rangle$ (with the output states represented by spheres) and $|V\rangle$ (with the output states represented by pyramids), respectively. The polarization ellipses illustrate the polarization state of each output channel. The colors of the polarization ellipses and the symbols on the Poincaré sphere correspond to the colors of the measured curves in (c). (c) The measured coincidence counts at 7 output channels ($CH_1, CH_2, \ldots, CH_7$) as a function of the rotation of QWP when the input single-photon states are $|H\rangle$ (dots) and $|V\rangle$ (triangles), respectively.

and the coincidence counts are recorded. The Stokes parameters are subsequently obtained by measuring coincidence counts as a function of the rotation angle of the QWP [62,63] (the input photon states are set as $|H\rangle$ and $|V\rangle$, respectively) [Fig. 2(c)]. The retrieved Stokes parameters in the Poincaré sphere [Fig. 2(b)] are either $|H\rangle$ or $|V\rangle$ states primarily located along the S_1 axis. The results are in agreement with the theoretical predictions, confirming that the metasurface has 7 output channels with different state transformations.

Next, we focus on demonstrating polarization entanglement and distribution by sending the photon pair generated by PPKTP to the metasurface. To check the stability of the photon source, we measure the coincidence count of the photon source over 100 min, and a fluctuation of about 0.87% has been detected [50]. A delay line and two PBSs ensure zero time delay between two photons. A narrow band spectral filter guarantees that two photons are indistinguishable in frequency (the bandwidth of our filter is 0.22 nm). The coincidence window is set to 1.5 ns to realize the postselection, and the coincidence count is collected continously for 20 s. To characterize the output state, we measure quantum state tomography (QST) [64], S parameter [65], and two-photon polarization interference fringes [17] of 21 channel pairs. In the measurements, the

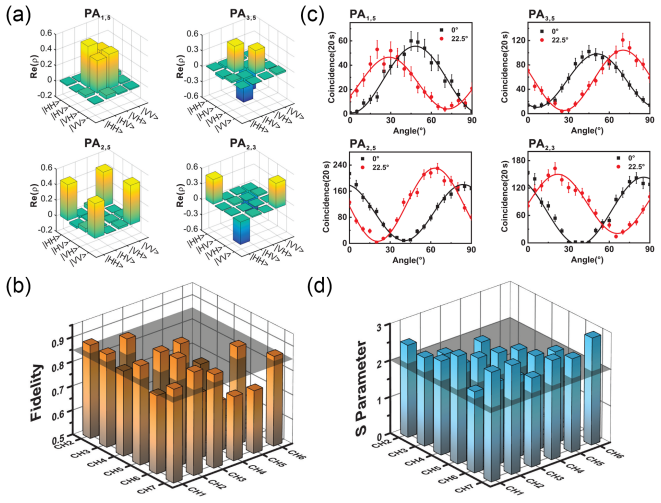

FIG. 3. Experimental demonstration of the generation of four Bell states and distribution to 21 channel pairs by the metasurface with $|HV\rangle$ incidence. (a) The real parts of the reconstructed density matrices of the entangled states distributed to $PA_{1,5}$, $PA_{3,5}$, $PA_{2,5}$, $PA_{2,3}$. (b) Measured fidelities of 21 states generated by the metasurface in Fig. 2. (c) Two-photon coincidence counts measured for 20 s at $PA_{1,5}$ (Ψ^+), $PA_{3,5}$ (Ψ^-), $PA_{2,5}$ (ϕ^+), and $PA_{2,3}$ (ϕ^-) as a function of the HWP angle placed behind one channel. The error bar is plotted assuming that the coincidence counts satisfy Poissonian photon statistics [6], which is the standard deviation of the count value of Ω ($\sqrt{\Omega}$). (d) S parameters of the entangled states distributed to all channel pairs.

background noise from accidental coincidence [66,67] has been subtracted. We reconstruct the density matrix with QST by applying the maximum likelihood estimation method [64] based on 16 measured two-photon coincidence counts. Figure 3(a) shows the real parts of the density matrices of four output states $|\Psi_{1,5}\rangle = \Psi^+$, $|\Psi_{3,5}\rangle = \Psi^-$, $|\Psi_{2,5}\rangle = \phi^+$, and $|\Psi_{2,3}\rangle = \phi^-$, and the information of the rest states are shown in [50]. The measured density matrices are in agreement with the matrices of the ideal states Ψ^+, Ψ^-, ϕ^+, and ϕ^-, respectively. The fidelity, which is defined as $F(\rho,\tilde{\rho}) = [\mathrm{Tr}(\sqrt{\tilde{\rho}^{1/2}\rho\tilde{\rho}^{1/2}})]^2$, with $\tilde{\rho}$ and ρ representing the reconstructed and expected density matrices, has been retrieved. The near-unity fidelity indicates that the entangled state is close to the desired state. Figure 3(b) shows the fidelities of 21 states, where most values are above 0.850, with an average of 0.847. The results confirm the occurrence of polarization entanglement in 21 channel pairs. In the current metasurface-based quantum system, the fidelity can be further improved by elaborately designing the unit cell and increasing the precision of nanofabrication to meet the stringent requirements of high-precision quantum network applications. An in-depth discussion of the factors affecting fidelity and potential strategies for improvement is provided in Supplemental Material [50].

To demonstrate the polarization correlation, we evaluate two-photon polarization interference fringes. Figure 3(c) shows the two-photon coincidence counts measured for 20 s at $PA_{1,5}$, $PA_{3,5}$, $PA_{2,5}$, and $PA_{2,3}$ as a function of the HWP angle placed in one channel (the data for the rest pairs are shown in [50]). The angle of HWP placed behind another channel is fixed at 0° (the dark curve) and 22.5° (the red curve) to project the photon onto $|H\rangle$ and $|R\rangle$ (right-handed circularly polarized) states [17]. Here we define the interference visibility as $\Lambda = [(C_{\max} - C_{\min})/(C_{\max} + C_{\min})]$, with $C_{\max}$ and $C_{\min}$ representing the maximum and minimum of the coincidence counts [17]. When HWP is rotated to 0° (22.5°), the calculated 21 (16) interference visibilities are all above 71%, suggesting Bell's inequality has been violated [65,68]. The results confirm the polarization correlation of the photon pairs collected from 21 channel pairs. Further, Clauser-Horne-Shimony-Holt (CHSH) inequality [65] has been tested, and S parameters are provided in Fig. 3(d). The S parameter of each channel pair is greater than 2, signifying that the CHSH inequality has been violated and the quantum states are entangled [65]. The results of QST, two-photon polarization interference fringes, and S parameters confirm the generation and distribution of four Bell states in 21 channel pairs.

Our strategy offers flexibility in generating entangled photon pairs by adjusting the input photon states or modifying the metasurface. Once the input state varies, the output state at $PA_{m,n}$ will be changed accordingly. When the input two-photon state changes from $|HV\rangle$ to $|AD\rangle$, where $|A\rangle = (\sqrt{2}/2)\binom{1}{-1}$ is −45° linearly polarized and $|D\rangle = (\sqrt{2}/2)\binom{1}{1}$ is +45° linearly polarized, the output state turns to $|\Psi_{m,n}\rangle = (\hat{J}_m|A\rangle \otimes \hat{J}_n|D\rangle + \hat{J}_m|D\rangle \otimes \hat{J}_n|A\rangle)/\sqrt{2}$. The same metasurface in Fig. 2 still generates 4 Bell states and distributes them to 21 channel pairs, which differ from those in Fig. 3. Meanwhile, the distribution to $PA_{1,4}$, $PA_{1,5}$, $PA_{2,6}$, $PA_{3,7}$, $PA_{4,5}$ becomes $(|HH\rangle - |VV\rangle)/\sqrt{2}$, the state distributed to $PA_{1,3}$, $PA_{1,7}$, $PA_{3,4}$, $PA_{3,5}$, $PA_{4,7}$, $PA_{5,7}$ is $(|HH\rangle + |VV\rangle)/\sqrt{2}$, distribution to $PA_{1,2}$, $PA_{1,6}$, $PA_{2,4}$, $PA_{2,5}$, $PA_{4,6}$, $PA_{5,6}$ is $(|HV\rangle - |VH\rangle)/\sqrt{2}$, and the remaining 4 channel pairs ($PA_{2,3}$, $PA_{2,7}$, $PA_{3,6}$, $PA_{6,7}$) are in $(|HV\rangle + |VH\rangle)/\sqrt{2}$ [Fig. 4(a)]. Experimentally, the input states $|AD\rangle$ have been obtained by rotating HWP in front of the metasurface, and reconstructing 21 quantum states with QST. The reconstructed density matrices of four output states $|\Psi_{3,7}\rangle = \phi^-$, $|\Psi_{1,7}\rangle = \phi^+$, $|\Psi_{1,6}\rangle = \Psi^-$, and $|\Psi_{6,7}\rangle = \Psi^+$ are illustrated in Fig. 4(b), while the rest of the states are shown in [50]. The retrieved fidelities are plotted in Fig. 4(c), where most values are above 0.840, with an average of 0.829.

The distribution of entangled photon states can also be modulated by modifying the assembly of nanocuboids in the unit cell. As illustrated in [50], the distribution of the entangled states can be tuned by keeping the silicon cuboid

(a)

Channel Pair / Input State	$PA_{1,4}$	$PA_{1,5}$	$PA_{2,6}$	$PA_{1,3}$	$PA_{1,7}$	$PA_{3,4}$	$PA_{1,2}$	$PA_{1,6}$	$PA_{2,4}$	$PA_{2,3}$	$PA_{2,7}$
	$PA_{3,7}$		$PA_{4,5}$	$PA_{3,5}$	$PA_{4,7}$	$PA_{5,7}$	$PA_{2,5}$	$PA_{4,6}$	$PA_{5,6}$	$PA_{3,6}$	$PA_{6,7}$
$\|HV\rangle$	ψ^+			ψ^-			ϕ^+			ϕ^-	
$\|AD\rangle$	ϕ^-			ϕ^+			ψ^-			ψ^+	

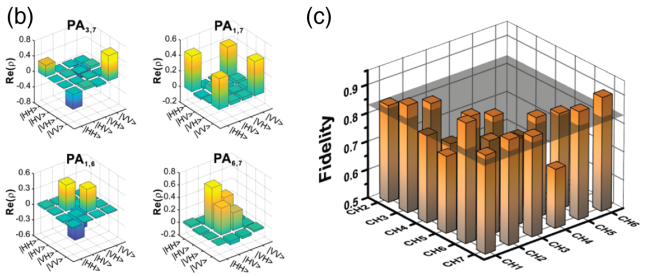

FIG. 4. (a) The table showing the output state at each channel pair when the input state is in $|HV\rangle$ and $|AD\rangle$, respectively. (b) The real parts of the reconstructed density matrices of four output states in QST measurement, $|\Psi_{3,7}\rangle = (|HH\rangle - |VV\rangle)/\sqrt{2}$, $|\Psi_{1,7}\rangle = (|HH\rangle + |VV\rangle)/\sqrt{2}$, $|\Psi_{1,6}\rangle = (|HV\rangle - |VH\rangle)/\sqrt{2}$, and $|\Psi_{6,7}\rangle = (|HV\rangle + |VH\rangle)/\sqrt{2}$. (c) The measured fidelities of 21 states generated by the metasurfaces in Fig. 2 when the input two-photon state changes to $|AD\rangle$.

in the unit cell while interchanging the orientation angles of the cuboids in two subsets following the rules $0 \leftrightarrow \pi/4$ and $\pi/2 \leftrightarrow 3\pi/4$. It follow that the distributed states to $PA_{1,4}$, $PA_{1,5}$, $PA_{2,6}$, $PA_{3,7}$, $PA_{4,5}$ become Ψ^+, the distribution to $PA_{1,3}$, $PA_{1,7}$, $PA_{3,4}$, $PA_{3,5}$, $PA_{4,7}$, and $PA_{5,7}$ becomes ϕ^+, the state to $PA_{1,2}$, $PA_{1,6}$, $PA_{2,4}$, $PA_{2,5}$, $PA_{4,6}$, $PA_{5,6}$ becomes Ψ^-, and the remaining 4 channels pairs ($PA_{2,3}$, $PA_{2,7}$, $PA_{3,6}$, $PA_{6,7}$) are in ϕ^-. Furthermore, the number of output channels can be expanded by increasing the number of nanocuboilds in the unit cell. For example, if the unit cell is enlarged by duplicating each nanocuboid in the unit cell following the same sequence in Fig. 2(a), the number of elements in the unit cell reaches 16. Accordingly, 13 output channels are generated, and the number of channel pairs jumps to 78 [50]. Therefore, the metasurface strategy will enhance the capacity and flexibility of a fully connected quantum network architecture.

As a cornerstone of quantum networking, the generation and distribution of various entangled photon pairs are essential for building fully connected quantum networks capable of efficient, reliable, and high-fidelity information exchanges. The nonlocal correlations intrinsic to entanglement underpin secure communication, enable advanced quantum information processing, and enhance fault tolerance through coordinated operations between different photon pairs. Traditionally, realizing these capabilities requires resource-intensive setups involving numerous (polarization) beam splitters and wave plates. In contrast, carefully engineered metasurfaces provide a compact, efficient, and highly controllable platform for integrated optical components in miniaturized quantum systems. By precisely manipulating the degrees of freedom of photons, metasurfaces enable versatile and interference-based control and distribution of quantum states. While spontaneous parametric down-conversion in nonlinear crystals remains the standard method for generating entangled photon pairs, metasurfaces offer distinct advantages in miniaturization and on-chip integration. For quantum networking applications, there is a growing demand for compact and robust platforms capable of generating diverse polarization-entangled photon pairs. Despite recent progress in metasurface-based quantum photonic devices, challenges remain in enhancing output fidelity, advancing integration with other photonic components, and achieving comprehensive control over photonic states. As a proof of concept, our Letter provides valuable insights into the design and realization of integrated entangled photon sources optimized for next-generation quantum networks.

To summarize, we demonstrate here an unprecedented advance in generating and distributing entangled quantum states across numerous channel pairs using a specially designed metasurface. By leveraging quantum interference at the metasurface, two orthogonally polarized photons become polarization entangled and are distributed to different output channels. This discovery illustrates the potential of metasurfaces in applications that require polarization entanglement among multiple photons and the distribution of entanglement across numerous users. This approach provides a compact and practical platform for high-capacity communication in quantum information processing, marking a significant step forward in quantum information science.

Acknowledgments—The authors gratefully acknowledge financial support from the National Key R&D Program of China (No. 2022YFA1404303 and No. 2020YFA0211300) and the National Natural Science Foundation of China (No. 12234010).

Data availability—The data that support the findings of this article are not publicly available. The data are available from the authors upon reasonable request.

[1] D. Bouwmeester, J.-W. Pan, K. Mattle, M. Eibl, H. Weinfurter, and A. Zeilinger, Experimental quantum teleportation, Nature (London) **390**, 575 (1997).
[2] X.-L. Wang, X.-D. Cai, Z.-E. Su, M.-C. Chen, D. Wu, L. Li, N.-L. Liu, C.-Y. Lu, and J.-W. Pan, Quantum teleportation of multiple degrees of freedom of a single photon, Nature (London) **518**, 516 (2015).
[3] J. Yin *et al.*, Entanglement-based secure quantum cryptography over 1,120 kilometers, Nature (London) **582**, 501 (2020).

[4] J. Wang, F. Sciarrino, A. Laing, and M. G. Thompson, Integrated photonic quantum technologies, Nat. Photonics **14**, 273 (2020).
[5] J. L. O'Brien, Optical quantum computing, Science **318**, 1567 (2007).
[6] M. Fox, *Quantum Optics* (Oxford University Press, New York, 2006).
[7] S. P. Neumann, A. Buchner, L. Bulla, M. Bohmann, and R. Ursin, Continuous entanglement distribution over a transnational 248 km fiber link, Nat. Commun. **13**, 6134 (2022).
[8] L. Agarwal, C. M. Langlett, and S. Xu, Long-range Bell states from local measurements and many-body teleportation without time reversal, Phys. Rev. Lett. **130**, 020801 (2023).
[9] K. Mattle, H. Weinfurter, P. G. Kwiat, and A. Zeilinger, Dense coding in experimental quantum communication, Phys. Rev. Lett. **76**, 4656 (1996).
[10] B. P. Williams, R. J. Sadlier, and T. S. Humber, Superdense coding over optical fiber links with complete Bell-state measurements, Phys. Rev. Lett. **118**, 050501 (2017).
[11] A. Karlsson, M. Koashi, and N. Imoto, Quantum entanglement for secret sharing and secret splitting, Phys. Rev. A **59**, 162 (1999).
[12] C.-M. Bai, S. Zhang, and L. Liu, Quantum direct secret sharing using Bell state, Laser Phys. Lett. **18**, 125204 (2021).
[13] P. D. Townsend, Quantum cryptography on multiuser optical fiber networks, Nature (London) **385**, 47 (1997).
[14] S. Wengerowsky, S. K. Joshi, F. Steinlechner, H. Hübel, and R. Ursin, An entanglement-based wavelength-multiplexed quantum communication network, Nature (London) **564**, 225 (2018).
[15] S. K. Joshi *et al.*, A trusted node-free eight-user metropolitan quantum communication network, Sci. Adv. **6**, eaba0959 (2020).
[16] S. Wehner, D. Elkouss, and R. Hanson, Quantum internet: A vision for the road ahead, Science **362**, eaam9288 (2018).
[17] P. G. Kwiat, K. Mattle, H. Weinfurter, and A. Zeilinger, New high-intensity source of polarization-entangled photon pairs, Phys. Rev. Lett. **75**, 4337 (1995).
[18] W. A. T. Nogueira, S. P. Walborn, S. Pádua, and C. H. Monken, Generation of a two-photon singlet beam, Phys. Rev. Lett. **92**, 043602 (2004).
[19] O. Kuzucu and F. N. C. Wong, Pulsed Sagnac source of narrow-band polarization-entangled photons, Phys. Rev. A **77**, 032314 (2008).
[20] R.-B. Jin, R. Shimizu, K. Wakui, M. Fujiwara, T. Yamashita, S. Miki, H. Terai, Z. Wang, and M. Sasaki, Pulsed Sagnac polarization-entangled photon source with a PPKTP crystal at telecom wavelength, Opt. Express **22**, 11498 (2014).
[21] S. M. Lee, H. Kim, M. Cha, and H. S. Moon, Polarization-entangled photon-pair source obtained via type-II non-collinear SPDC process with PPKTP crystal, Opt. Express **24**, 2941 (2016).
[22] H. Jin, F. M. Liu, P. Xu, J. L. Xia, M. L. Zhong, Y. Yuan, J. W. Zhou, Y. X. Gong, W. Wang, and S. N. Zhu, On-chip generation and manipulation of entangled photons based on reconfigurable lithium-niobate waveguide circuits, Phys. Rev. Lett. **113**, 103601 (2014).
[23] Z. Tang, B. Wang, T. Chen, and X. Zhang, Transmission and transformation of entangled states with high fidelity in a non-Hermitian system, Phys. Rev. Res. **4**, 043144 (2022).
[24] G. Guccione, T. Darras, H. L. Jeannic, V. B. Verma, S. W. Nam, A. Cavaillès, and J. Laurat, Connecting heterogeneous quantum networks by hybrid entanglement swapping, Sci. Adv. **6**, eaba4508 (2020).
[25] M. Pompili *et al.*, Realization of a multimode quantum network of remote solid-state qubits, Science **372**, 259 (2021).
[26] K. Edamatsu, Entangled photons: Generation, observation, and characterization, Jpn. J. Appl. Phys. **46**, 7175 (2007).
[27] H. Hübel, M. R. Vanner, T. Lederer, B. Blauensteiner, T. Lorünser, A. Poppe, and A. Zeilinger, High-fidelity transmission of polarization encoded qubits from an entangled source over 100 km of fiber, Opt. Express **15**, 7853 (2007).
[28] F. Steinlechner *et al.*, A high-brightness source of polarization-entangled photons optimized for applications in free space, Opt. Express **20**, 9640 (2012).
[29] Y. Xiao, X.-J. Ye, K. Sun, J.-S. Xu, C.-F. Li, and G.-C. Guo, Demonstration of multisetting one-way Einstein-Podolsky-Rosen steering in two-qubit systems, Phys. Rev. Lett. **118**, 140404 (2017).
[30] J. Liu, Q. Yang, Y. Shou, S. Chen, W. Shu, G. Chen, S. Wen, and H. Luo, Metasurface-assisted quantum nonlocal weak-measurement microscopy, Phys. Rev. Lett. **132**, 043601 (2024).
[31] M. W. Mitchell, C. W. Ellenor, S. Schneider, and A. M. Steinberg, Diagnosis, prescription, and prognosis of a Bell-state filter by quantum process tomography, Phys. Rev. Lett. **91**, 120402 (2003).
[32] J. W. Pan, Z.-B. Chen, C.-Y. Lu, H. Weinfurter, A. Zeilinger, and M. Żukowski, Multiphoton entanglement and interferometry, Rev. Mod. Phys. **84**, 777 (2012).
[33] C.-H. Wu, C.-K. Liu, Y.-C. Chen, and C.-S. Chuu, Revival of quantum interference by modulating the biphotons, Phys. Rev. Lett. **123**, 143601 (2019).
[34] I. Choi, R. J. Young, and P. D. Townsend, Quantum information to the home, New J. Phys. **13**, 063039 (2011).
[35] B. Fröhlich, J. F. Dynes, M. Lucamarini, A. W. Sharpe, Z. Yuan, and A. J. Shields, A quantum access network, Nature (London) **501**, 69 (2013).
[36] T.-Y. Chen *et al.*, Metropolitan all-pass and inter-city quantum communication network, Opt. Express **18**, 27217 (2010).
[37] X.-Y. Chang, D.-L. Deng, X.-X. Yuan, P.-Y. Hou, Y.-Y. Huang, and L.-M. Duan, Experimental realization of an entanglement access network and secure multi-party computation, Sci. Rep. **6**, 29453 (2016).
[38] D. Aktas, B. Fedrici, F. Kaiser, T. Lunghi, L. Labonté, and S. Tanzilli, Entanglement distribution over 150 km in wavelength division multiplexed channels for quantum cryptography, Laser Photonics Rev. **10**, 451 (2016).
[39] T. Stav, A. Faerman, E. Maguid, D. Oren, V. Kleiner, E. Hasman, and M. Segev, Quantum entanglement of the spin and orbital angular momentum of photons using metamaterials, Science **361**, 1101 (2018).

[40] K. Wang *et al.*, Quantum metasurface for multiphoton interference and state reconstruction, Science **361**, 1104 (2018).
[41] P. Georgi, M. Massaro, K.-H. Luo, B. Sain, N. Montaut, H. Herrmann, T. Weiss, G. Li, C. Silberhorn, and T. Zentgraf, Metasurface interferometry toward quantum sensors, Light Sci. Appl. **8**, 70 (2019).
[42] L. Li *et al.*, Metalens-array-based high-dimensional and multiphoton quantum source, Science **368**, 1487 (2020).
[43] Q. Li, W. Bao, Z. Nie, Y. Xia, Y. Xue, Y. Wang, S. Yang, and X. Zhang, A non-unitary metasurface enables continuous control of quantum photon-photon interactions from bosonic to fermionic, Nat. Photonics **15**, 267 (2021).
[44] T. S. Cruz, S. D. Gennaro, O. Mitrofanov, S. Addamane, J. Reno, I. Brener, and M. V. Chekhova, Resonant metasurfaces for generating complex quantum states, Science **377**, 991 (2022).
[45] J. Zhang, J. Ma, M. Parry, M. Cai, R. Camacho-Morales, L. Xu, D. N. Neshev, and A. A. Sukhorukov, Spatially entangled photon pairs from lithium niobate nonlocal metasurfaces, Sci. Adv. **8**, eabq4240 (2022).
[46] Y.-J. Gao, Z. Wang, Y. Jiang, R.-W. Peng, Z.-Y. Wang, D.-X. Qi, R.-H. Fan, W.-J. Tang, and M. Wang, Multichannel distribution and transformation of entangled photons with dielectric metasurfaces, Phys. Rev. Lett. **129**, 023601 (2022).
[47] Z. Wang, Y. Jiang, Y.-J. Gao, R.-H. Fan, D.-X. Qi, R. Zhong, H.-L. Zhang, R.-W. Peng, and M. Wang, Implement quantum tomography of polarization-entangled states via nondiffractive metasurfaces, Appl. Phys. Lett. **121**, 081703 (2022).
[48] Y.-J. Gao, X. Xiong, Z. Wang, F. Chen, R.-W. Peng, and M. Wang, Simultaneous generation of arbitrary assembly of polarization states with geometrical-scaling-induced phase modulation, Phys. Rev. X **10**, 031035 (2020).
[49] Y.-J. Gao, Z. Wang, W. Tang, X. Xiong, Z. Wang, F. Chen, R.-W. Peng, and M. Wang, Metasurface design for the generation of an arbitrary assembly of different polarization states, Phys. Rev. B **104**, 125419 (2021).
[50] See Supplemental Material at http://link.aps.org/supplemental/10.1103/mzmv-7x98 for further theoretical and experimental details, which includes Refs. [51–60].
[51] A. Arbabi, Y. Horie, M. Bagheri, and A. Faraon, Dielectric metasurfaces for complete control of phase and polarization with subwavelength spatial resolution and high transmission, Nat. Nanotechnol. **10**, 937 (2015).
[52] Y. H. Shih and C. O. Alley, New type of Einstein-Podolsky-Rosen-Bohm experiment using pairs of light quanta produced by optical parametric down conversion, Phys. Rev. Lett. **61**, 2921 (1988).
[53] C. E. Kuklewicz, M. Fiorentino, G. Messin, F. N. C. Wong, and J. H. Shapiro, High-flux source of polarization-entangled photons from a periodically poled $KTiOPO_4$ parametric down-converter, Phys. Rev. A **69**, 013807 (2004).
[54] S. M. Barnett, On single-photon and classical interference, Phys. Scr. **97**, 114004 (2022).
[55] W.-H. Lee, High efficiency multiple beam gratings, Appl. Opt. **18**, 2152 (1979).
[56] N. M. Estakhri and A. Alù, Wave-front transformation with gradient metasurfaces, Phys. Rev. X **6**, 041008 (2016).
[57] N. Gisin, G. Ribordy, W. Tittel, and H. Zbinden, Quantum cryptography, Rev. Mod. Phys. **74**, 145 (2002).
[58] R. Kaltenbaek and B. Blauensteiner, Experimental interference of independent photons, Phys. Rev. Lett. **96**, 240502 (2006).
[59] T. Kobayashi, R. Ikuta, S. Yasui, S. Miki, T. Yamashita, H. Terai, T. Yamamoto, M. Koashi, and N. Imoto, Frequency-domain Hong-Ou-Mandel interference, Nat. Photonics **10**, 441 (2016).
[60] T. Baumgratz, M. Cramer, and M. B. Plenio, Quantifying coherence, Phys. Rev. Lett. **113**, 140401 (2014).
[61] T. B. Pittman, D. V. Strekalov, A. Migdall, M. H. Rubin, A. V. Sergienko, and Y. H. Shih, Can two-photon interference be considered the interference of two photons?, Phys. Rev. Lett. **77**, 1917 (1996).
[62] D. H. Goldstein, *Polarized Light* (CRC Press, Boca Raton, FL, 2017).
[63] M. Mohammadi, A. M. Brańczyk, and D. F. V. James, Fourier-transform quantum state tomography, Phys. Rev. A **87**, 012117 (2013).
[64] D. F. V. James, P. G. Kwiat, W. J. Munro, and A. G. White, Measurement of qubits, Phys. Rev. A **64**, 052312 (2001).
[65] J. F. Clauser and A. Shimony, Bell's theorem. Experimental tests and implications, Rep. Prog. Phys. **41**, 1881 (1978).
[66] K. J. Resch, P. Walther, and A. Zeilinger, Full characterization of a three-photon Greenberger-Horne-Zeilinger state using quantum state tomography, Phys. Rev. Lett. **94**, 070402 (2005).
[67] P. Y. Hou, Y.-Y. Huang, X.-X. Yuan, X.-Y. Chang, C. Zu, L. He, and L.-M. Duan, Quantum teleportation from light beams to vibrational states of a macroscopic diamond, Nat. Commun. **7**, 11736 (2016).
[68] J. Zhou, S. Liu, H. Qian, Y. Li, H. Luo, S. Wen, Z. Zhou, G. Guo, B. Shi, and Z. Liu, Metasurface enabled quantum edge detection, Sci. Adv. **6**, eabc4385 (2020).